# Using Activated Biochar from *Caryocar brasiliense* Pequi Almonds for Removing Methylene Blue Dye in an Aqueous Solution

André Luiz Ferreira Carvalho Melo [1], Marcelo Teixeira Carneiro [1], Alan Ícaro Sousa Morais [2], Bartolomeu Cruz Viana [2], Francisco Eroni Paz Santos [2], Josy Anteveli Osajima [2], Roosevelt D. S. Bezerra [3], Ramón Raudel Peña-Garcia [4], Luciano C. Almeida [4], Santiago Medina Carrasco [5] and Edson C. Silva-Filho [2,*]

1 Federal Institute of Piauí, Campus Floriano, Floriano 64800-000, PI, Brazil; andreluiz@ifpi.edu.br (A.L.F.C.M.); marcelo.teixeira@ifpi.edu.br (M.T.C.)
2 Interdisciplinary Laboratory for Advanced Materials, Federal University of Piauí, Teresina 64049-550, PI, Brazil; alanicaro@gmail.com (A.Í.S.M.); bartolomeu@ufpi.edu.br (B.C.V.); franciscoeroni@gmail.com (F.E.P.S.); josyosajima@ufpi.edu.br (J.A.O.)
3 Federal Institute of Piauí, Teresina-Central Campus, Teresina 64000-060, PI, Brazil; rooseveltdsb@ifpi.edu.br
4 Academic Unit of Cabo de Santo Agostinho, Rural Federal University of Pernambuco, Cabo de Santo Agostinho, Pernambuco 54518-430, PE, Brazil; rraudelp@gmail.com (R.R.P.-G.); luciano.calmeida@ufpe.br (L.C.A.)
5 X-ray Laboratory (CITIUS), Universidad de Sevilla, Avenida Reina Mercedes, 4B, 41012 Sevilla, Spain; sanmedi@us.es
* Correspondence: edsonfilho@ufpi.edu.br

**Abstract:** Water pollution remains a global problem that urges researchers to develop new technologies aimed at environmental restoration. Here, this study aimed at obtaining an activated biochar from pequi almonds for dye removal. Before and after adsorption, the materials underwent characterization using techniques such as X-ray diffraction (XRD), Fourier transform infrared spectroscopy (FTIR), scanning electron microscopy (SEM), Raman spectroscopy, and thermogravimetric analysis (TG). The biochar from the pequi almond was called BA, and the activated biochar from the pequi almond was called ABA. The influence of the pH, contact time, and adsorbate concentration on adsorption was investigated using the dye methylene blue. The morphological assessment revealed higher cracks and pores in the ABA than in the BA. The TG showed that the BA lost approximately 19% more mass than the ABA, indicating that activation occurred. The activation contributed to the decrease in the degree of disorder in the BA because of the increased number of graphitic carbon atoms (ordered) in the ABA, as observed via Raman. The adsorption kinetics followed a pseudo-second-order model, while the adsorption isotherms followed the Langmuir model. The BA adsorption capacity was 500.00 mg g$^{-1}$, constituting a robust solution for dye removal from aqueous environments. Therefore, this implies the success of the process.

**Keywords:** water treatment; chemical activation; adsorption; methylene blue; pequi almond biochar; NaOH-activated biochar

## 1. Introduction

Industries contribute significantly to the world economy; however, they can generate effluents that, if left untreated, can cause damage to the environment. Primary effluents such as phenols, dyes, heavy metals, solid waste in suspension, and different gases are the main sources of harm to the water quality [1,2]. Synthetic dyes in effluents cause adverse effects on the ecosystem and human health, leading to an imbalance in aquatic ecosystems and degradation of the water source quality [3,4].

Methylene blue (MB) is a cationic dye extensively employed in textiles, paints, and pharmaceuticals. Due to its extensive utilization, this dye is frequently identified in effluent

and aquatic environments. Human exposure to water containing this dye can result in various health concerns, such as eye and skin irritation, seizures, rapid heart rate, shortness of breath, and, upon ingestion, may lead to gastrointestinal irritation, nausea, and occasionally diarrhea [5–7].

The scientific community is greatly concerned about the environmental pollution from the food, cosmetic, pharmaceutical, and textile industries. Researchers have been engaged in studies that propose approaches for addressing these pollutants. These approaches encompass various techniques, including advanced oxidation technologies, chemical oxidation, chemical precipitation, membrane separation, coagulation, and adsorption [2,6,8,9].

The adsorption process is an accessible alternative for treating several types of effluents, including those from the textile industries, due to its economical production and the lack of secondary byproducts, thus making this approach advantageous [10,11].

Biochar production involves using plant-derived materials (biomass), which contain renewable lignocellulosic materials such as plant residues, sawdust, and fruit components that exhibit varying degrees of porosity [12–15].

Among the biomass residues investigated for repurposing in biochar production, the pequi nut (*Caryocar brasiliense*), a distinctive fruit from the Brazilian Cerrado region, stands out. The pequi holds notable economic significance due to its utilization in cooking and the production of liqueurs and medicinal syrups. Furthermore, studies in the literature have shown that adsorbents produced from pequi (*Caryocar brasiliense*) efficiently remove dyes, heavy metals, and herbicides from an aqueous medium due to their differentiated physical and chemical properties [15–18]. Thus, it is crucial to conduct further studies on using almonds derived from pequi, which commonly appear as production waste, to produce adsorbents to remove contaminants from aqueous environments. In this way, because it is a typical Cerrado fruit, with great abundance in several states of Brazil, is low-cost, has no toxicity, and has promising adsorbent properties, almond emerges as a promising biomass candidate for biochar manufacturing [19–22].

We aimed to produce and activate biochar using biomass residues (specifically, pequi almonds (seed)). These materials were characterized using different equipment and subsequently employed in adsorption tests to remove a model organic dye. The experiments involved variations in parameters such as the pH, time, and concentration, and the acquired data were fitted to mathematical models of kinetics and equilibrium.

## 2. Experimental Part

### 2.1. Reagents

The reagents used were methylene blue (MB) ($C_{16}H_{18}Sn_3Cl$, Dinâmica, Brazil, 97%), sodium hydroxide (NaOH, Dinâmica, 98%), hydrochloric acid (HCl, Dinâmica, 38%), sodium chloride (NaCl, Dynamics, 99%), and distilled water. The reagents were used without purification. Pequi almond residues were purchased at the market in Floriano, State of Piauí (PI), specifically on Avenida Bucar Neto, Centro, ZIP Code 64800-000.

### 2.2. Biochar Preparation

Biochar production from pequi almonds was executed through a sequential four-stage procedure (Figure 1). In the initial stage, the gathering of pequi and the physical elimination of unwanted elements were performed. The different components of pequi (mesocarp, endocarp, and almond) were segregated, with the almonds being subjected to a 2 h drying period under sunlight ($30 \pm 2$ °C). The dried almonds were processed in a mill and sieved through a sieve (stainless steel sieve—ASTM 10—MESH/TYLER 9—2 mm opening). The material was subjected to oven-drying in the third phase and transferred to porcelain crucibles for carbonization. The carbonization process occurred within a muffle furnace (model CE–800/S–4) with a gradual heating rate of 10 °C per minute (°C min$^{-1}$) until reaching a temperature of 500 °C for 30 min. Afterwards, the material was allowed to cool down to room temperature with a cooling rate of 10 °C min$^{-1}$. The product was called pequi almond biochar (BA). BA underwent chemical activation. The activating agent

used in the chemical activation process was sodium hydroxide (NaOH), using the ratio 1:3 (*w:w*). In other words, one part BA plus three parts NaOH were used. Thus, the BA biochar was physically mixed with NaOH. Initially, a mixture of biochar and precursor was produced, which underwent a thermal activation treatment (TAT), gradually increasing the temperature at 5 °C min$^{-1}$ until it reached 800 °C. Then, a controlled cooling process was implemented at a rate of 5 °C min$^{-1}$. The material subjected to TAT was washed with distilled water and HCl (1.0 mol/L) to remove excess NaOH. After the immersion, the material obtained was separated through filtration and subjected to a drying period of 12 h at 105 °C in an oven. The activation procedure was called activated pequi almond biochar (ABA) [18,23,24].
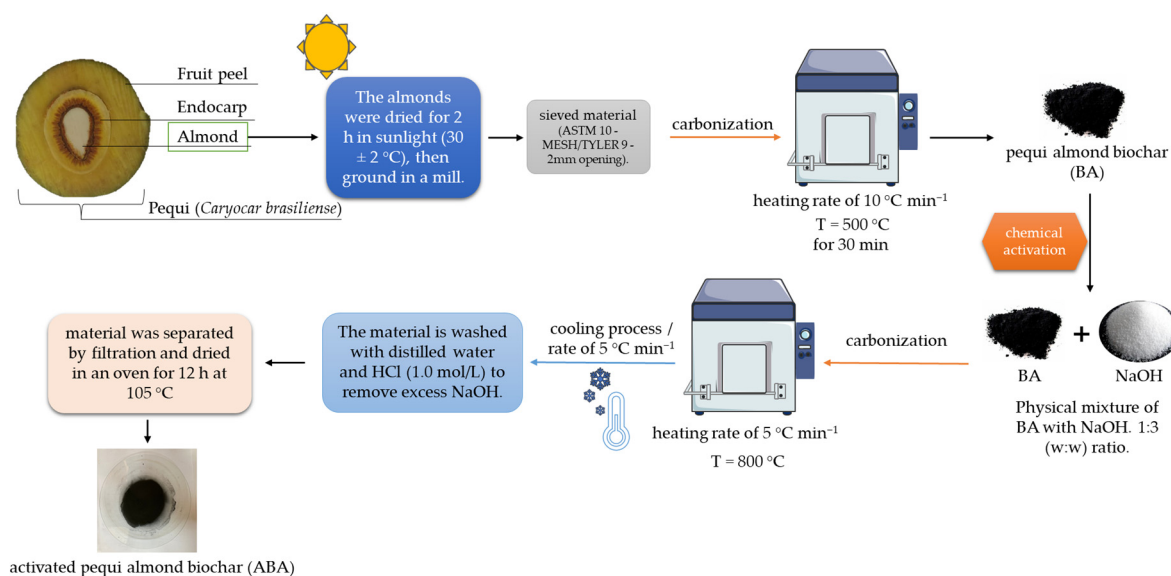


**Figure 1.** Production of biochar derived from pequi almonds.

### 2.3. Characterizations

Infrared spectra were acquired employing a Bomem FTIR spectrophotometer, MB series, utilizing the wafer method. The data collection encompassed 60 scans, spanning the range of 600 to 4000 cm$^{-1}$. Thermal analysis was performed using a Shimadzu DT-60 thermal analyzer. The analysis was conducted under an inert nitrogen atmosphere, employing a heating rate of 10 °C min$^{-1}$ within the 25 to 800 °C temperature range. X-ray diffraction (XRD) analysis was performed using a Shimadzu instrument, model Labx-XDR 6000, covering a scan range of $2\theta = 3°$ to $75°$. Raman spectra were acquired employing a Raman spectrometer (Horiba-Jobin-Yvon, LabRam HR Evolution, Frankfurt, Germany). The excitation source was a solid emitter (785 nm) with a laser beam power set at 1 mW. Each acquisition involved an exposure time of 30 s and was averaged over ten accumulations. A 50x magnification lens was employed during the measurement. The full width determined the curve fitting utilizing Lorentz and Gauss functions at half maximum (FWHM), peak position, and intensity. Porosity characterization, encompassing specific surface area, pore diameter, and total pore volume, was conducted through N$_2$ adsorption/desorption isotherm analysis at 77 K. The analysis was performed utilizing a micrometer (ANOVA 1000e—Quantachrome Autosorb-iQ Instruments), employing both the Brunauer–Emmett–Teller (BET) and Barrett–Joyner–Halenda (BJH) methods.

### 2.4. Point of Zero Charge (pH$_{PZC}$)

Determining the pH at the point of zero charge (pH$_{PZC}$) involves balancing the adsorbent's surface charge and the solution's charge. First, 20.0 mg of biochar was introduced into 20.0 mL of NaCl solution (0.1 mol L$^{-1}$), and the pH was adjusted within the pH range of 2 to 10. We used 1.0 mol L$^{-1}$ HCl and/or 1.0 mol L$^{-1}$ NaOH solutions for necessary

adjustments. The mixtures were stirred at 140 rpm and maintained at 25 °C for 24 h on an orbital shaker table with temperature control (TE-420 INCUBADORA-TECNAL, Limeira, Brazil), with the equipment used in the following experiments. The solutions underwent centrifugation for 10 min at a speed of 5000 rpm (NI 1812 Benchtop Centrifuge—Piracicaba, NOVA Instruments, Brazil). The solutions were centrifuged at 5000 rpm for 10 min, and the final pH was measured (pHmeter Model: PHS-3E—EVEN). The $\Delta pH$ value was calculated using Equation (1), the initial pH values (referred to as $pH_0$), and the final $pH$ (referred to as $pH_0$). The dataset was employed to construct a plot correlating $\Delta pH$ against $pH_0$. The point at $\Delta pH$ equating to 0 indicates zero charges [25].

$$\Delta pH = pH_0 - pH_f \tag{1}$$

### 2.5. The Influence of pH

The impact of pH on dye adsorption was systematically explored in triplicate at pH values of 4, 7, and 10. Then, 40 mg of biochar (BA or ABA) was added in the methylene blue (MB) dye solution (20.0 mL). The MB concentration was 100.0 mg L$^{-1}$ using BA and 800 mg L$^{-1}$ using ABA. After 24 h of contact time, the solutions were centrifuged. The concentrations were determined using a calibration curve established in a UV-Vis spectrophotometer (Agilent Cary 60 UV-Vis spectrophotometer), with the wavelength used being 663 nm, referring to the maximum wavelength of the MB dye. Equation (2) was used to determine the adsorbed quantity $q_e$ (mg g$^{-1}$) [15,25].

$$q_e = \frac{\left(C_i - C_f\right)}{m} \cdot V \tag{2}$$

$C_i$ signifies the initial dye concentration (mg L$^{-1}$), while $C_f$ stands for the final concentration (mg L$^{-1}$). The variable $m$ represents the mass of the adsorbent, measured in grams, and $V$ denotes the volume of dye solution, in liters [15,25].

### 2.6. Adsorption Kinetics

The kinetic evaluation of the adsorption was carried out in triplicate at a temperature of 25 °C, with the pH adjusted according to the result of the previous section, The Influence of pH, with the value used referring to the highest adsorption capacity. In separate flasks, 40 mg of biochar was added to 20.0 mL of MB dye solution. The dye concentration used for BA was 100 mg L$^{-1}$, while for ABA, it was 800 mg L$^{-1}$.

The solutions were agitated at 140 rpm for a pre-established time. Afterwards, the samples were centrifugated. The adsorbed quantification was calculated using Equation (2). The data were fitted to pseudo-first-order and pseudo-second-order kinetic models, respectively (Equations (3) and (4)) [26,27].

$$ln(q_e - q_t) = lnq_e - k_1 \cdot t \tag{3}$$

$$\frac{t}{q_t} = \frac{1}{k_2 \cdot q_e^2} + \frac{t}{q_e} \tag{4}$$

where $q_e$ signifies the quantities of adsorbed dye (mg g$^{-1}$) at equilibrium, and $q_t$ signifies the quantities of adsorbed dye (mg g$^{-1}$) at equilibrium time $t$ (minutes). The parameter $k_1$ denotes the adsorption constant of the pseudo-first-order model (min$^{-1}$), while $k_2$ represents the constant associated with the pseudo-second-order kinetic model (mg g$^{-1}$ min$^{-1}$).

### 2.7. Adsorption Isotherm

The concentration variation was measured in triplicate at 25 °C, using pH and time adjustments optimized for maximum adsorption. In the initial stage, 40.0 mg of biochar (BA or ABA) was added to a dye solution containing 20.0 mL. The dye concentration

range was 50 to 1000 mg L$^{-1}$ for the BA material and 1000 to 1600 mg L$^{-1}$ for the ABA material. After the contact time, aliquots were centrifuged (and if necessary, diluted). Then, the equilibrium concentrations were calculated using Equation (2). Finally, the adsorption isotherm model that best fits the experimental data—Langmuir or Freundlich—was identified. The linearized form of the Langmuir equation via Equations (5) and (6) presents the linearized version of the Freundlich equation [28,29].

$$\frac{C_e}{q_e} = \frac{1}{K_L \cdot q_0} + \frac{C_e}{q_0} \tag{5}$$

$$lnqe = lnK_F + \frac{1}{n}lnC_e \tag{6}$$

Within these equations, $q_e$ refers to the amount of substance adsorbed per unit mass of the adsorbent (mg g$^{-1}$), and $q_0$ represents the maximum adsorption capacity per unit mass of the adsorbent (mg g$^{-1}$). $C_e$ represents the adsorbate equilibrium concentration (mg L$^{-1}$), $K_L$ symbolizes the Langmuir adsorption constant associated with the chemical equilibrium between adsorbate and adsorbent (mg L$^{-1}$), $K_F$ represents the Freundlich adsorption constant, and $n$ is a parameter related to the strength of the adsorption process.

## 3. Results and Discussions

The obtained biochar materials had the characteristic of a fine, low-density black gunpowder, which is characteristic for this material. Figure 2a presents the X-ray diffractograms for the BA and ABA. The analysis classifies the biochar (BA) as amorphous, and the activated biochar (ABA) exhibits low crystallinity. Some peaks demonstrate the difference and activation effect, indicating a different organization after activation. The XRD for the ABA has two peaks at 2θ = 20° and 2θ= 25°, which may indicate the presence of carbon structures [30]. It can also be observed that some peaks indicate a degree of gratification of the material, which in this case would be the peaks at 2θ = 22.24° and 43.36°, referring to the (002) and (100) graphitic plane [31,32]. The structure of the activated biochar forms stacks of parallel graphene layers that make up tiny fragments of graphene planes plus disorganized amounts of carbon [33].

The FTIR spectra of the pequi almond biochar (BA) and and activated pequi almond biochar (ABA) are shown in Figure 2b. The BA presented bands in the 1130, 889, and 577 cm$^{-1}$ regions. These bands are related to C-O-C stretching, C-H deformation of aromatics, and C-C-H bending, respectively, as they are these bands' characteristics of biochars [34].

Changes are evident in the spectra of the activation process. The band intensity at the 1083 cm$^{-1}$ region indicates CO vibrations typically associated with oxidized biochars. A new band emerges at 470 cm$^{-1}$, corresponding to C-O-H bending, a characteristic feature of activated biochar. The shift can be attributed to the biochar activation procedure, underscoring inherent structural alterations [18,34].

The thermogravimetric analysis (TG) for the biochars (BA and ABA) are presented in Figure 2c. c1 and c3 in Figure 2 represent the TG profiles of the BA and ABA, respectively, while the derivatives of the corresponding thermogravimetric curves (DTG) are also presented (as c2 and c4 in Figure 2). The thermal behavior was divided into distinct stages: three stages for the BA and two stages for the ABA. The initial stage occurs at approximately 50 °C for the ABA and 75 °C for the BA. A decrease in mass is attributed to the release of trapped water and physically adsorbed gases. The BA phase, around 624 °C, possibly indicates the expulsion of molecules confined in the material's pores. The third stage of the BA process occurs around 917 °C, representing the highest degradation rate of the material. The second stage for the ABA occurs at a temperature of 930 °C, indicating the existence of aromatic compounds within the material after the adsorption procedure [35,36]. When analyzing the residual mass, the BA material (67.5%) lost about 19% more mass than the residual mass of the ABA material (86.5%). This reinforces the successful occurrence of activation, underscoring the imperative role of biochar activation in eliminating impurities and molecules encapsulated in the material [37].

Figure 2d shows the $pH_{PZC}$ curves of the biochar. The $pH_{PZC}$ value of the BA biochar was 8.3, and the $pH_{PZC}$ of the ABA biochar was 5.5. The presence of molecules that were removed with the activation shown in the TG curves caused impairments in the functional groups because they were physically adsorbed, causing a lower acidity on the BA surface.
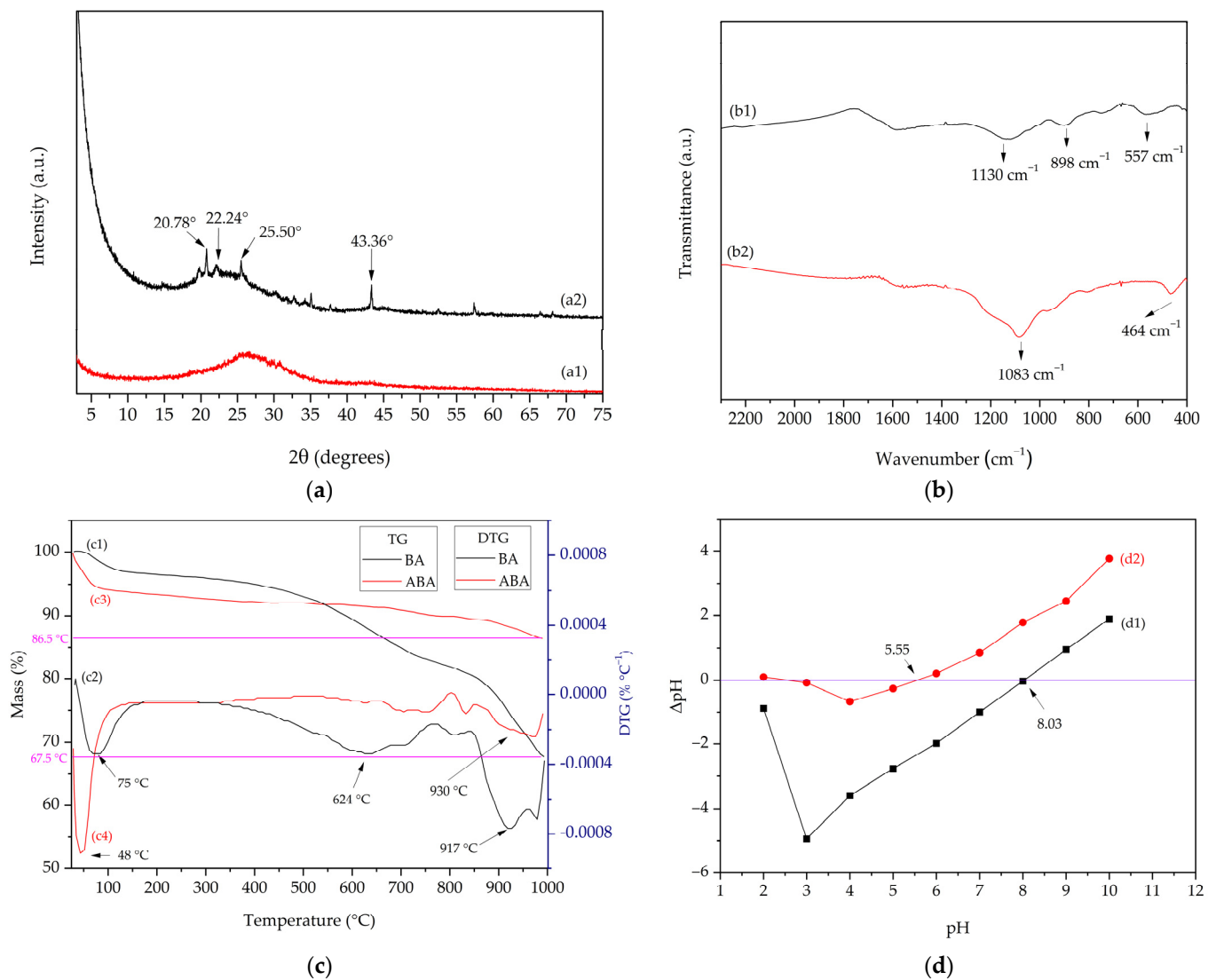


**Figure 2.** Characterization analysis of almond biochar (BA) and activated almond biochar (ABA): (**a**) XRD diffractogram of pequi almond biochar (BA) (a1) and activated pequi almond biochar (ABA) (a2); (**b**) FTIR spectra of pequi almond biochar (BA) (b1) and activated pequi almond biochar (ABA) (b2); (**c**) thermal analysis, TG (c1) and DTG (c2), for pequi almond biochar (BA) and TG (c3) and DTG (c4) for activated pequi almond biochar (ABA); (**d**) pH point of zero charge ($pH_{PZC}$) for pequi almond biochar (BA) (d1) and activated pequi almond biochar (ABA) (d2).

The morphological assessment of the biochars is shown in Figure 3, employing various magnifications to examine their shapes and surface characteristics. The visual representations of the BA biochar are presented in Figure 3A,B, illustrating three-dimensional particles that coalesce into nonhomogeneous blocks with limited pore distribution. In contrast, the images of the ABA biochar (Figure 3D,E) reveal blocks exhibiting a more pronounced pore population than the BA biochar. The result aligns with the TG and $pH_{PZC}$ values, indicating the sites with organic molecules. The distinction becomes more evident in Figure 3C,F, wherein the ABA biochar manifests more significant cracks and pores than the BA. It is, according to previous results, reaffirming the activation's success. The non-uniform config-

urations of the ABA biochar exhibit irregular shapes, potentially contributing positively to the adsorption capacity [38,39].
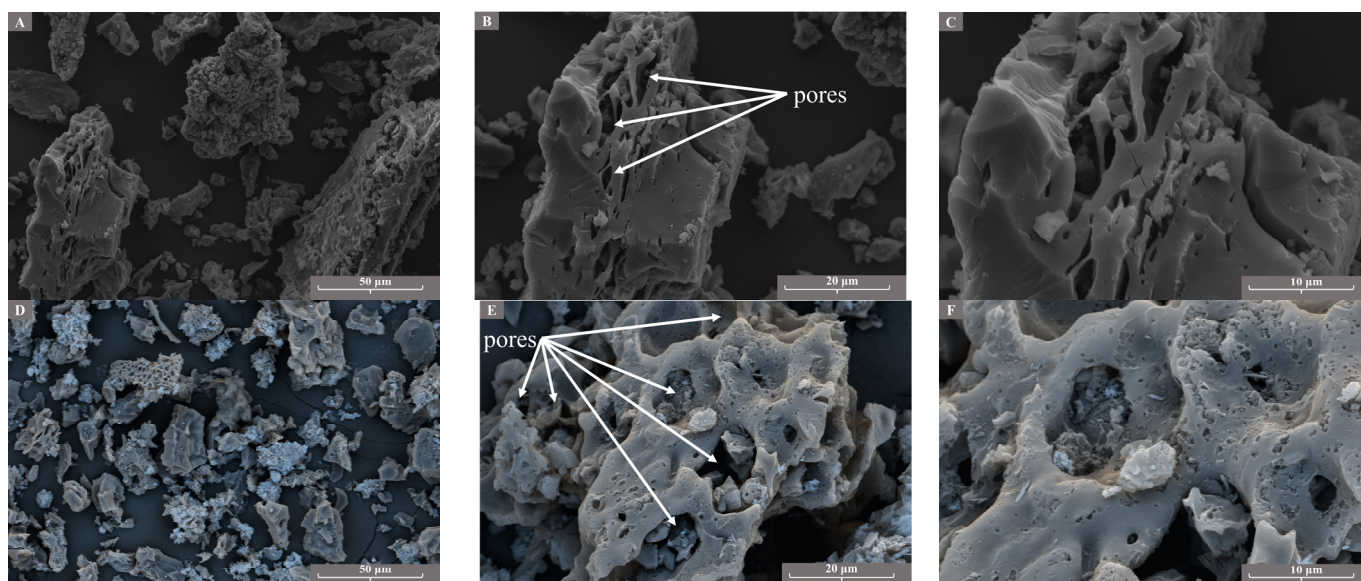


**Figure 3.** Scanning electron microscopy (SEM) images of the BA sample with a scale size of 50 μm (**A**), 20 μm (**B**), and 10 μm (**C**), and the ABA sample with a scale size of 50 μm (**D**), 20 μm (**E**), and 10 μm (**F**).

Figure 4 presents the Raman spectra for the BA (Figure 4a) and ABA (Figure 4b) samples. All Raman spectra were obtained with excitation at 785 nm and show characteristic bands of carbonized samples. The linear fit of the Raman curves shows two prominent bands. The D1 band is associated with disordered carbon atoms and is typically around 1350 cm$^{-1}$ [40]. Moreover, the G band is associated with graphitic carbon atoms (ordered), typically around 1580 cm$^{-1}$ [41]. The intensity ratio of these two bands, I(D1)/I(G), measures the degree of disorder in activated carbon, with a higher ratio indicating more disorder. The results are summarized in Table 1.
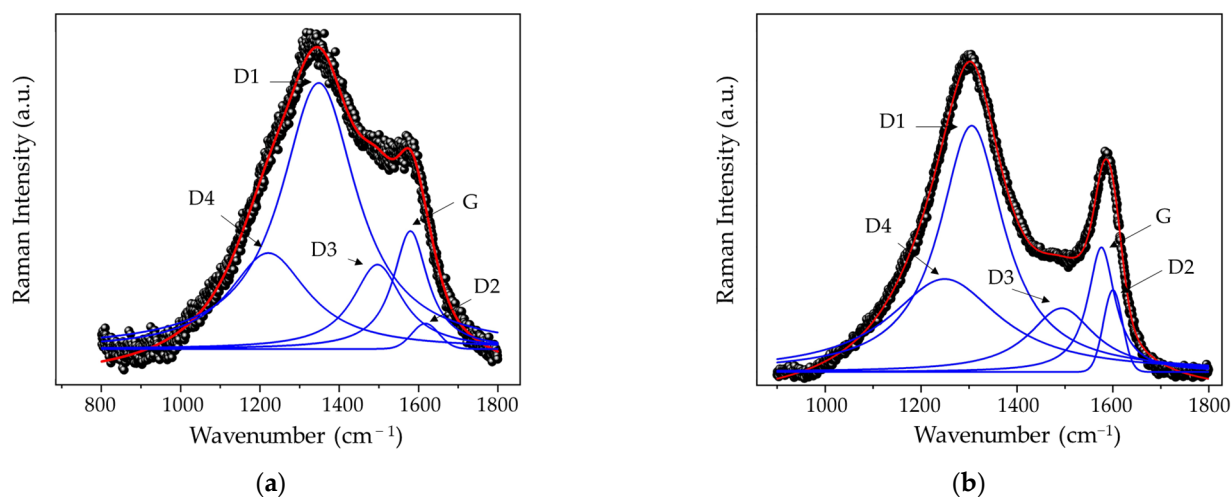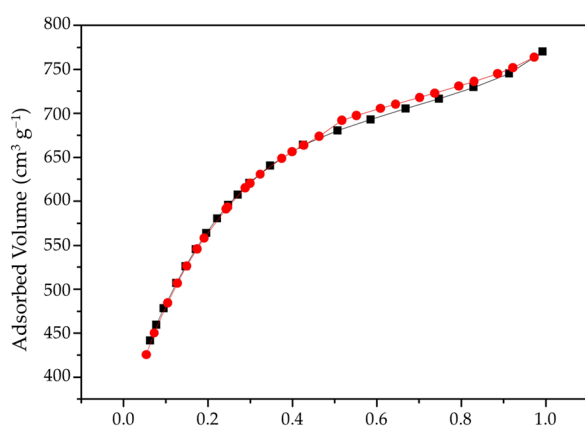


(**a**)

(**b**)

**Figure 4.** *Cont*.

(**c**)

**Figure 4.** Raman spectra of BA (**a**) ABA (**b**). The scatter are experimental data, the fits are the solid red line, and solid blue lines are the deconvolution using Lorentzian peaks fitted to the spectrum representing each Raman mode. The nitrogen adsorption/desorption isotherm ($N_2$) for ABA (**c**).

**Table 1.** The intensity ratio of I(D1)/I(G) bands for BA and ABA biochars.

| Bands | BA Biochar | | | ABA Biochar | | |
|---|---|---|---|---|---|---|
| | Amplitude | Center | FWHM | Amplitude | Center | FWHM |
| D1 | 182.48 | 1348.40 | 230.98 | 295.87 | 1305.55 | 162.46 |
| G | 80.82 | 1579.41 | 106.11 | 149.71 | 1576.07 | 68.65 |
| ID1/IG | | 2.26 | | | 1.98 | |

The nitrogen adsorption/desorption isotherm ($N_2$) for ABA is shown in Figure 4c. The isotherm is Type IV, a mesoporous structure in the biochar and monolayer–multilayer adsorption with a hysteresis loop at a high relative pressure H4. The nitrogen volume adsorption in the lower pressure range ($0 < p/p0 < 0.5$) increased smoothly, showing monolayer adsorption. The gas adsorption gradually increased ($0.5 < p/p0 < 0.8$), indicating that the adsorption shifted from monolayer to multilayer. The interval of ($0.8 < p/p0 < 1.0$) was observed for gas adsorption, which strongly indicates the occurrence of a capillary condensation phenomenon during the adsorption process. The textural characteristics of the BA and ABA adsorbents are shown in Table 2 [42].

**Table 2.** $N_2$ adsorption/desorption information—surface area, pore volume, and average pore diameter for BA and ABA biochars.

| Biochar | Surface Area $m^2\ g^{-1}$ | Pore Volume—BJH $cm^3\ g^{-1}$ | Average Pore Diameter—BJH (nm) |
|---|---|---|---|
| BA | 14.5 | 0.093 | 3.115 |
| ABA | 1923.0 | 0.290 | 3.133 |

The intensity ratio of the I(D1)/I(G) bands for the BA biochar is 2.26, whereas for the ABA biochar, it is 1.98. The results indicate that the activation process contributed to a decrease in the degree of disorder in the biochar, increasing the number of graphitic carbon atoms (ordered) in the ABA [43], corroborating the data obtained via the XRD, in which the activation generated a different organization and was an amorphous material before the activation.

Table 2 presents the BA and ABA biochars surface area, pore volume, and mean pore diameter values. Specifically, for the BA, the surface area is 14.5 $m^2\ g^{-1}$, the pore volume is 3.115 nm, and the pore diameter is 0.093 $cm^3\ g^{-1}$. In contrast, the ABA exhibits significantly

higher values, with a surface area of 1923.0 m$^2$ g$^{-1}$, pore volume of 3.133 nm, and mean pore diameter of 0.290 cm$^3$ g$^{-1}$. This indicates a significant increase in the surface area and pore volume values of the ABA biochar compared with those of the BA, which was expected to improve the MB adsorption process. Additionally, the average pore diameters of the BA (3.115 nm) and ABA (3.133 nm) classify the biochars as mesoporous. These results confirm that the ABA has a large surface area and mesopores and can be considered a potential adsorbent for dyes [44,45].

Figure 5 shows the variation in adsorbed amounts concerning the pH in the study of the pH dependence of the MB solution. The most efficient removal of MB dye by the BA biochar is consistently achieved at pH 4 and 7. Consequently, pH 7 was chosen for subsequent tests. On the other hand, an increase in MB adsorption by the ABA biochar is discernible at pH 10. As a result, pH 10 was selected for the following assays. It is known that for biochar, pHpzc values are characterized by the material's surface being positive, and for values above pHpzc, the material's surface is negatively charged [46]. Thus, according to the results presented in the figure about the pHpzc of the BA and ABA biochars, they emphasize the reason for the difference in adsorption presented under the influence of pH, with the amount adsorbed by the BA being 12 mg g$^{-1}$, while for the ABA, it was 464 mg g$^{-1}$ at pH 10. This shows that the ABA material having a negative surface charge favors adsorption via electrostatic attraction between the MB dye and the surface of the activated biochar when used in more alkaline pH liquids. The activation process applied to biochar derived from Pequi almonds is advantageous.
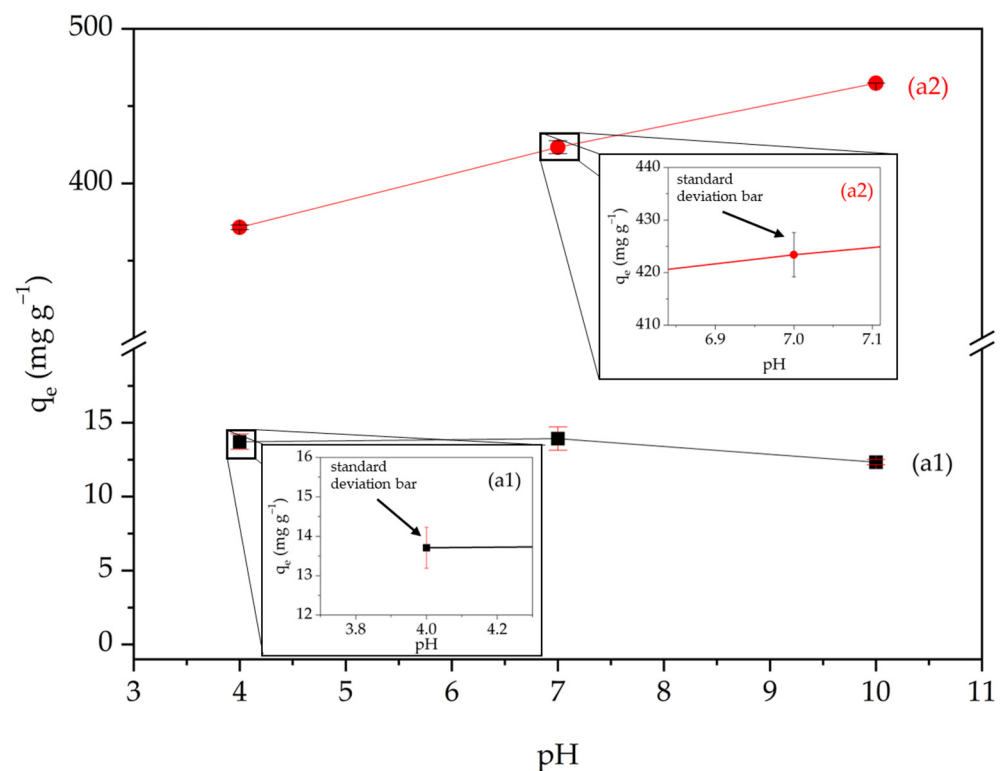


**Figure 5.** Correlation between adsorbed dye amount for BA (a1) and ABA (a2) as a function of pH.

The kinetics of the adsorption for both the BA and ABA are illustrated in Figure 6a and were fitted using the pseudo-first-order (PFO) and pseudo-second-order (PSO) models. The assessment of the isothermal adsorption for the biochars is presented in Figure 6b and was fitted using the Langmuir and Freundlich models. The linearized versions of these models were analyzed through the correlation coefficient (R$^2$) and the parameters of their adjustments (Tables 3 and 4).

**Figure 6.** Adsorption kinetics for BA (a1) and ABA (a2) (**a**); concentration isotherm for BA (b1) and ABA (b2) (**b**).

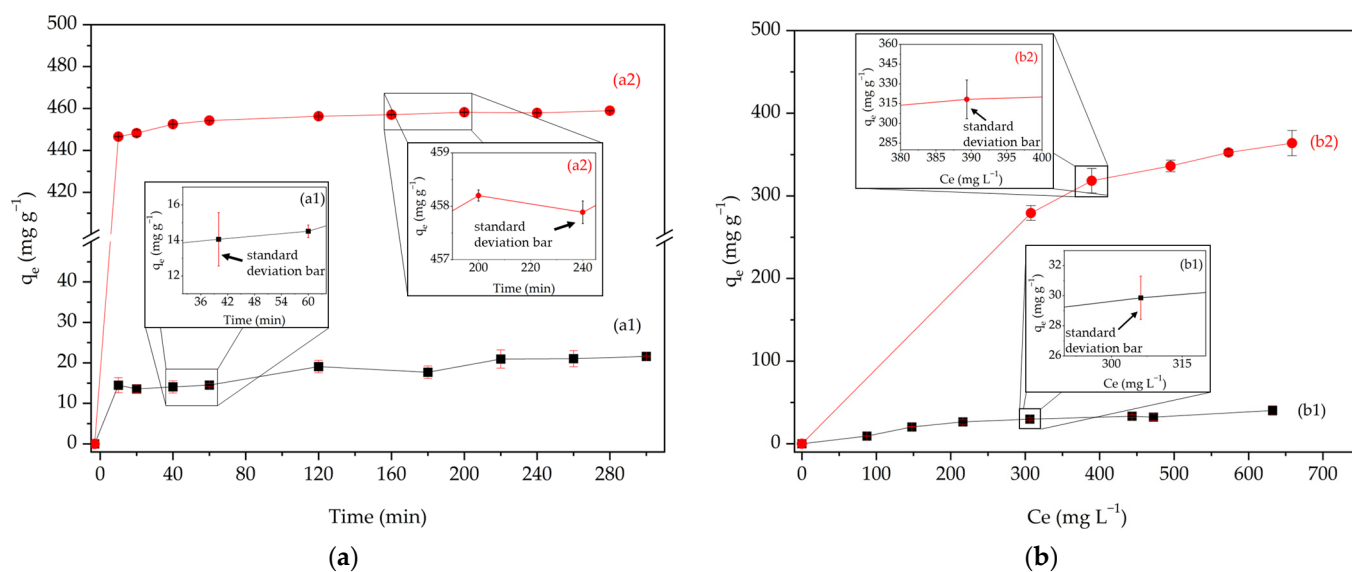**Table 3.** Fitting to the pseudo-first-order and pseudo-second-order kinetic models for the BA and ABA biochars.

| Biochar | Pseudo-First-Order | | | Pseudo-Second-Order | | |
|---------|---------------------|---|---|----------------------|---|---|
| | $q_e$ (mg g$^{-1}$) | $K_1$ (min$^{-1}$) | $R^2$ | $q_e$ (mg g$^{-1}$) | $K_2$ (mg g$^{-1}$ min$^{-1}$) | $R^2$ |
| BA | 11.20 | 0.0098 | 0.8850 | 22.32 | 0.0022 | 0.9844 |
| ABA | 11.75 | 0.0084 | 0.9453 | 500.00 | 0.0040 | 0.9999 |

**Table 4.** Fitting to the Langmuir and Freundlich isothermal models for BA and ABA biochars.

| Biochar | Langmuir | | | Freundlich | | |
|---------|----------|---|---|------------|---|---|
| | $q_0$ | $K_L$ | $R^2$ | $n$ | $K_F$ | $R^2$ |
| BA | 42.73 | 0.009992 | 0.9268 | 11.0497 | 18.05 | 0.1846 |
| ABA | 476.19 | 0.004671 | 0.9965 | 2.9797 | 41.73 | 0.9643 |

The acquired kinetic data underwent comparison with two distinct kinetic models: the pseudo-first-order and the pseudo-second-order. The comparison enabled an exploration of the adsorption process rate and the determination of the rate-controlling step governing the adsorption of the MB within the biochars. The adsorption stabilization occurs within approximately 15 min. As depicted in Table 3, the pseudo-second-order (PSO) model presents the most fitting description of the biochar's MB adsorption process in both scenarios, attributed to the notably high correlation coefficient values ($R^2$), reaching 0.9844 for the BA and 0.9999 for the ABA. The calculated $q_e$ results from the PSO model closely align with the experimental $q_e$ values, underscoring that the MB dye's adsorption transpired via chemical interactions involving the functional groups on the material's surface. The analysis revealed a substantial disparity in adsorption between the ABA and BA. The adsorption capacity ($q_e$) for the ABA reached an impressive 500.00 mg g$^{-1}$, significantly surpassing the performance of the BA, which registered a $q_e$ of 22.32 mg g$^{-1}$. This stark difference underscores the efficacy of the chemical activation process, solidifying its utility in dye removal from aqueous environments. The results of the kinetic tests, combined with the analysis of surface charges and the differences in the biochars' morphological

characteristics, indicate that the activation process was a success [47,48]. Furthermore, it is essential to point out that these results for the BA and ABA are similar to those found in the literature for biochars and activated biochars used in MB adsorption [15,18,49,50]. The concentration variation adsorption test at constant temperature of biochars (Figure 6b) reveal an enhancement in adsorption capacity. These isotherms were fitted to the Langmuir and Freundlich models. The linearized versions of the Langmuir and Freundlich models were scrutinized utilizing the correlation coefficient ($R^2$), with the respective statistical attributes presented in Table 4.

Table 4 demonstrates that the Langmuir isotherm model more accurately characterizes the MB adsorption process by the biochars in both cases. The correlation coefficient ($R^2$) values were 0.9268 for the BA and 0.9965 for the ABA. The adsorption process occurred on the surface of the adsorbent in a uniform monolayer configuration and through chemical interactions, as in the kinetic results. The correlation values for the BA indicated a relatively lower alignment with the model. This can be attributed to molecules on the surface before activation, which may have caused less uniform adsorption in sites than the adsorption in the ABA, which was better adjusted to the Langmuir model, with values closer to 1 for the ABA (Figure 7). The experimental values for each biochar, presented in Figure 6b, follow a concave curve, typical of microporous carbons, which presents an increase in the initial concentrations, indicating a strong affinity for dye with the materials, followed by a saturation, which is characteristic of the Langmuir isotherms [51,52].
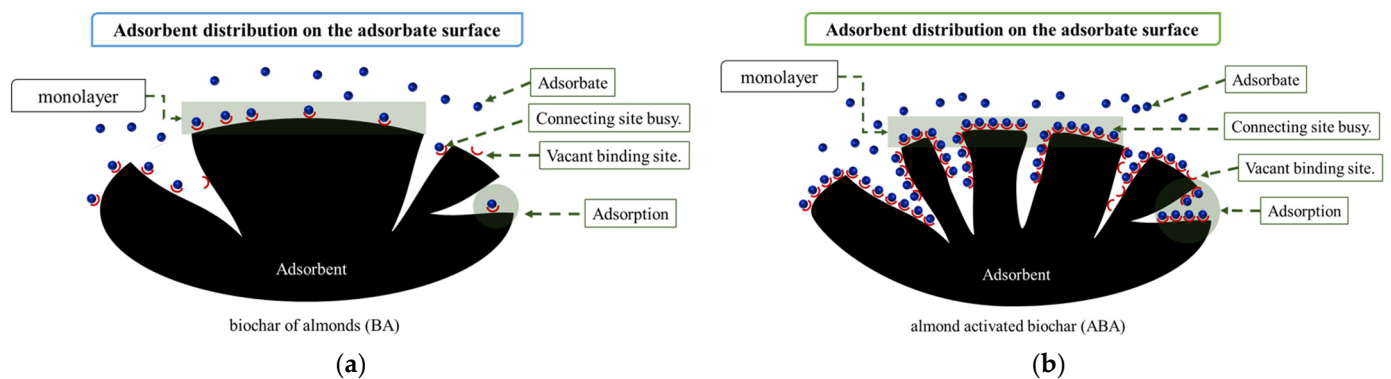


**Figure 7.** Mechanism of MB adsorption on biochars BA (**a**) and ABA (**b**).

*Characterization of Biochars after Adsorption*

After the adsorption of the dye, the materials were characterized to verify changes in their properties and validate the binding of the dye to the biochars. The same initials were used to facilitate identification by adding "A" after the initials of the material, i.e., BAA and ABAA for the pequi almond biochar after adsorption and activated pequi almond biochar after adsorption, respectively.

The FTIR spectra of the materials after adsorption (Figure 8a) showed significant results. The band in the two studied biochars, around 1100 cm$^{-1}$, is attributed to symmetrical C–O–C stretching vibrations after adsorption [53]. The band around 470 cm$^{-1}$ in the ABA biochar, representing a C = O bond, disappeared after the adsorption process, probably due to the interaction with the MB [54]. The bands remained around 900 cm$^{-1}$ for the BAA material, which is attributed to the C-H bond [55,56].

The thermal analysis of the BA biochar, before and after adsorption, is represented in Figure 8b. The thermal profile of the biochar remains similar to that observed before adsorption. However, noticeable differences are evident between the curves before and after adsorption. The mass difference between the two curves corresponds to the adsorbed dye, providing clear evidence of the effectiveness of the adsorption process. This indicates the successful impregnation of the dye onto the material's surface. At 1000 °C, the BA biochar has 67.7% mass, while the BAA has 57.9%. Therefore, there is a difference in the mass percentage of about 9.8%, which refers to the mass of the adsorbed dye. The result

shows a proportional percentage to the adsorbed amount, corroborating the adsorption efficiency of the MB by the BA shown in the adsorptive studies.
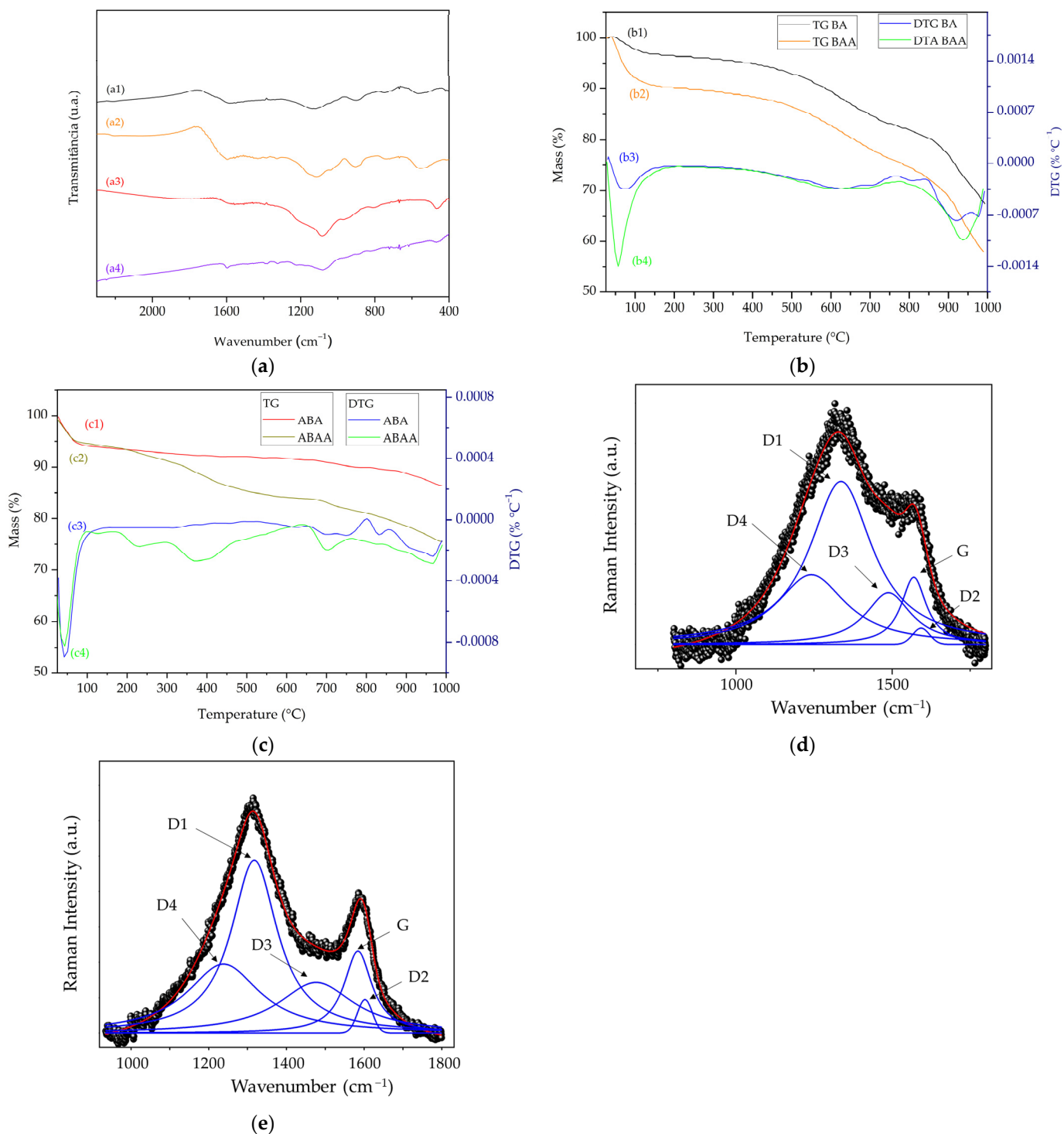


**Figure 8.** FTIR for the coal samples from BA(a1), BAA(a2), ABA(a3), and ABAA(a4) (**a**); TG (b1) and DTG (b3) curves for the studied BA samples and TG (b2) and DTG (b4) curves for the studied BAA samples (**b**); TG (c1) and DTG (c3) curves for the studied ABA samples and TG (c2) and DTG (c4) curves for the studied ABAA samples (**c**); Raman spectra for BAA (**d**) and ABAA (**e**).

Analyzing the ABA and ABAA curves (as depicted in Figure 8c), it becomes evident that these curves experienced a noteworthy alteration in terms of mass loss, while the

temperature ranges remained unchanged. At 1000 °C, the ABA biochar has 86.25% mass, while the ABAA has 75.67%. Therefore, there is a difference in the mass percentage of about 11%. This increment is directly proportional to the quantity of adsorbed dye. The methodology effectively immobilized the dye on the surface, and the quantity adsorbed following activation surpassed that of the biochar. The analysis after adsorption shows a strong indication of the interaction between the dye and the biochars, reinforcing the adsorption data and corroborating the other techniques [18,57].

The Raman spectra of the BAA biochars (Figure 8d) and ABAA biochars (Figure 8e) showed Gaussian and Liptizian curves similar to those of the BA biochars (Figure 4a) and the ABA (Figure 4b). The linear fit of the Raman curves shows the permanence of two prominent bands, one associated with disordered carbon atoms around 1350 cm$^{-1}$ and another associated with graphitic carbon atoms (ordered) around 1580 cm$^{-1}$ [58]. The intensity ratio of the I(D1)/I(G) bands for the BAA and ABAA biochar is shown in Table 5.

**Table 5.** The intensity ratio of the I(d)/I(g) bands for the BAA and ABAA biochars.

| Bands | BAA Biochar | | | ABAA Biochar | | |
|---|---|---|---|---|---|---|
| | Amplitude | Center | FWHM | Amplitude | Center | FWHM |
| D1 | 202.72 | 1336.65 | 244.42 | 122.01 | 1317.40 | 144.73 |
| G | 83.69 | 1569.68 | 97.55 | 57.88 | 1584.28 | 87.26 |
| ID1/IG | 2.42 | | | 2.11 | | |

Table 5, compared with Table 1, shows an increase in the intensity ratio of the I(D1)/I(G) bands. The intensity ratio of the I(D1)/I(G) bands for the BA biochar before adsorption is 2.26. After adsorption, it is 2.42, whereas the intensity ratio of the I(D1)/I(G) bands for the ABA biochar before adsorption is 1.98, and after adsorption, it is 2.11. Raman spectra were used to assess the degree of defects (D peaks) and graphitic arrangements (G peaks) in the biochars before and after dye adsorption. After the adsorption of MB molecules, the intensity ratio (ID/IG) increased, suggesting definite interactions between the dye and the biochar and increasing the disorder in the system [59]. Figure 9 shows the hysteresis of the ABA biochar (before adsorption) and the ABAA (after adsorption). After adsorption, the hysteresis loop remains, meaning that the isotherms remain type IV [60].
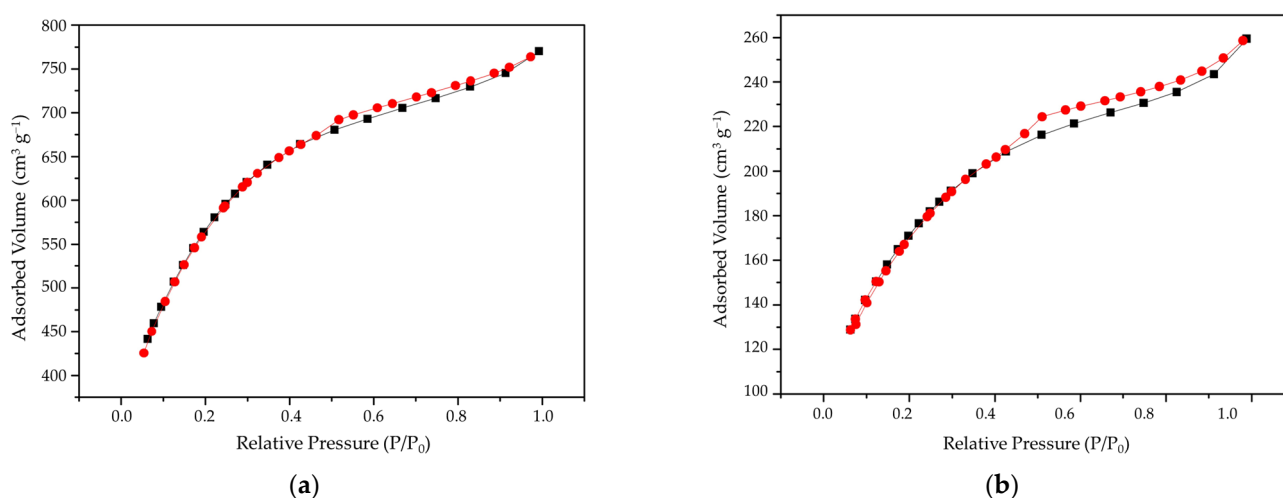


**Figure 9.** BET for ABA (**a**) and ABAA (**b**) samples.

Table 6 presents the surface area, pore volume, and average pore diameter measurements for the different biochar samples: BA, BAA, ABA, and ABAA. The observed parameter variations reflect the distinct structural characteristics of the activation processes

and applied impregnation techniques. The volume and surface area of the biochar decrease from $0.093$ cm$^3$ g$^{-1}$ (BA) to $0.027$ cm$^3$ g$^{-1}$ (BAA) and from $14.5$ m$^2$ g$^{-1}$ (BA) to $13.4$ m$^2$ g$^{-1}$ (BAA), indicating the presence of MB after biochar adsorption. The results also show that the pore volume and surface area decreased considerably from $0.290$ cm$^3$ g$^{-1}$ (ABA) to $0.134$ cm$^3$ g$^{-1}$ (ABAA) and from $1923.0$ m$^2$ g$^{-1}$ (ABA) to $598.6$ m$^2$ g$^{-1}$ (ABAA), demonstrating the presence of MB and the consequent efficiency of the biochar adsorption process. The reduction in the BET surface area and pore volume after adsorption is apparent, proving once again that the MB adsorption process on the surface of the biochars occurred satisfactorily [61].

**Table 6.** Surface area, pore volume, and average pore diameter of BA, BAA, ABA, and ABAA biochars.

| Biochar | Surface Area m$^2$ g$^{-1}$ | Pore Volume—BJH cm$^3$ g$^{-1}$ | Average Pore Diameter—BJH (nm) |
|---|---|---|---|
| BA | 14.5 | 0.093 | 3.115 |
| BAA | 13.4 | 0.027 | 3.180 |
| ABA | 1923.0 | 0.290 | 3.133 |
| ABAA | 598.6 | 0.134 | 3.957 |

## 4. Conclusions

Pequi almond biochar was successfully prepared through biomass pyrolysis at 500 °C. The biochar underwent an efficient activation process, with NaOH at 800 °C as the activating agent, which was proven by the characterizations with changes in structure, changes in thermal profile, the removal of some impurities present before activation, and the change in some bands in the FTIR due to the removal of some groups following from activation. The intensity ratio of the I(D1)/I(G) bands, made via the Raman study, confirms that the activation process contributed to the reduction in the degree of the biochar, increasing the graphitic carbon atoms (ordered) in the TAB. The biochar application to methylene blue (MB) adsorption remarkably adhered to the pseudo-second-order kinetic and Langmuir isothermal models. The most substantial adsorption capacities were recorded at pH 10 for the ABA and within the pH range of 4 to 7 for the BA. Notably, the activated material derived from renewable biomass, naturally discarded without established utility, emerged as a promising adsorbent for effectively eliminating dyes from aqueous settings. With an outstanding adsorption capacity of $500.00$ mg g$^{-1}$ for methylene blue, this study underscores the compelling potential of harnessing such sustainable sources to generate high-performance biochar materials, offering substantial prospects for sustainable environmental solutions.

**Author Contributions:** Conceptualization, A.L.F.C.M., M.T.C., A.Í.S.M. and E.C.S.-F.; Formal analysis, A.L.F.C.M., M.T.C., A.Í.S.M., F.E.P.S. and R.D.S.B.; Investigation, A.L.F.C.M., M.T.C., A.Í.S.M. and R.D.S.B.; methodology, A.L.F.C.M., M.T.C. and A.Í.S.M.; Project administration, A.L.F.C.M., A.Í.S.M. and E.C.S.-F.; software, A.L.F.C.M., M.T.C. and A.Í.S.M.; validation, A.L.F.C.M., M.T.C., A.Í.S.M. and R.D.S.B.; data curation, A.L.F.C.M. and A.Í.S.M.; Visualization, A.L.F.C.M., M.T.C., A.Í.S.M., F.E.P.S., J.A.O., R.D.S.B., R.R.P.-G., L.C.A. and S.M.C.; investigation, A.L.F.C.M., M.T.C. and A.Í.S.M.; resources, B.C.V., J.A.O., R.D.S.B., R.R.P.-G., L.C.A., S.M.C. and E.C.S.-F.; writing—original draft preparation, A.L.F.C.M., M.T.C. and A.Í.S.M.; writing—review and editing, A.L.F.C.M., M.T.C., A.Í.S.M., B.C.V., F.E.P.S., J.A.O., R.D.S.B., R.R.P.-G., L.C.A., S.M.C. and E.C.S.-F.; supervision, E.C.S.-F.; funding acquisition, J.A.O. and E.C.S.-F. All authors have read and agreed to the published version of the manuscript.

**Conflicts of Interest:** The authors declare no conflict of interest.

## References

1. Ahmad, R.; Ansari, K. Enhanced Sequestration of Methylene Blue and Crystal Violet Dye onto Green Synthesis of Pectin Modified Hybrid (Pect/AILP-Kal) Nanocomposite. *Process Biochem.* **2021**, *111*, 132–143. [CrossRef]
2. Zaman, K.U.; Abbas, N.; Irshad, M.; Zehra, S.; Butt, M.T.; Shehzad, K.; Mahmood, H.R. Treatability Study of Synthesized Silica Nanoparticles to Reduce Pollution Load of Industrial Wastewater. *Int. J. Environ. Sci. Technol.* **2022**, *19*, 6183–6200. [CrossRef]
3. Lum, P.T.; Foo, K.Y.; Zakaria, N.A.; Palaniandy, P. Ash Based Nanocomposites for Photocatalytic Degradation of Textile Dye Pollutants: A Review. *Mater. Chem. Phys.* **2020**, *241*, 122405. [CrossRef]
4. Nguyen, D.T.C.; Vo, D.V.N.; Nguyen, T.T.; Nguyen, T.T.T.; Nguyen, L.T.T.; Tran, T.V. Kinetic, Equilibrium, Adsorption Mechanisms of Cationic and Anionic Dyes on N-Doped Porous Carbons Produced from Zeolitic-Imidazolate Framework. *Int. J. Environ. Sci. Technol.* **2022**, *19*, 10723–10736. [CrossRef]
5. Jawad, A.H.; Abdulhameed, A.S.; Mastuli, M.S. Mesoporous Crosslinked Chitosan-Activated Charcoal Composite for the Removal of Thionine Cationic Dye: Comprehensive Adsorption and Mechanism Study. *J. Polym. Environ.* **2020**, *28*, 1095–1105. [CrossRef]
6. Oraon, A.; Prajapati, A.K.; Ram, M.; Saxena, V.K.; Dutta, S.; Gupta, A.K. Synthesis, Characterization, and Application of Microporous Biochar Prepared from *Pterospermum acerifolium* Plant Fruit Shell Waste for Methylene Blue Dye Adsorption: The Role of Surface Modification by SDS Surfactant. *Biomass Convers. Biorefin.* **2022**. [CrossRef]
7. Prajapati, A.K.; Mondal, M.K. Comprehensive Kinetic and Mass Transfer Modeling for Methylene Blue Dye Adsorption onto CuO Nanoparticles Loaded on Nanoporous Activated Carbon Prepared from Waste Coconut Shell. *J. Mol. Liq.* **2020**, *307*, 112949. [CrossRef]
8. Ali, I.; Basheer, A.A.; Mbianda, X.Y.; Burakov, A.; Galunin, E.; Burakova, I.; Mkrtchyan, E.; Tkachev, A.; Grachev, V. Graphene Based Adsorbents for Remediation of Noxious Pollutants from Wastewater. *Environ. Int.* **2019**, *127*, 160–180. [CrossRef]
9. Mingming, L.; Jing, G.; Piao, Y.; Liu, D.; Jin, L. Treatment of Refractory Organic Pollutants in Industrial Wastewater by Wet Air Oxidation. *Arab. J. Chem.* **2017**, *10*, S769–S776.
10. Hadj-Otmane, C.; Ouakouak, A.; Touahra, F.; Grabi, H.; Martín, J.; Bilal, M. Date Palm Petiole–Derived Biochar: Effect of Pyrolysis Temperature and Adsorption Properties of Hazardous Cationic Dye from Water. *Biomass Convers. Biorefin.* **2022**. [CrossRef]
11. Reza, M.S.; Afroze, S.; Bakar, M.S.A.; Saidur, R.; Aslfattahi, N.; Taweekun, J.; Azad, A.K. Biochar Characterization of Invasive *Pennisetum purpureum* Grass: Effect of Pyrolysis Temperature. *Biochar* **2020**, *2*, 239–251. [CrossRef]
12. Hsu, D.; Lu, C.; Pang, T.; Wang, Y.; Wang, G. Adsorption of Ammonium Nitrogen from Aqueous Solution on Chemically Activated Biochar Prepared from Sorghum Distillers Grain. *Appl. Sci.* **2019**, *9*, 5249. [CrossRef]
13. Gümüş, F. Utilization of Algal Waste Biomass-Derived Biochar Prepared by a Microwave-Assisted Method for Aniline Green Adsorption. *Water Air Soil Pollut.* **2022**, *233*, 364. [CrossRef]
14. Vijayaraghavan, K.; Ashokkumar, T. Characterization and Evaluation of Reactive Dye Adsorption onto Biochar Derived from *Turbinaria Conoides* Biomass. *Environ. Prog. Sustain. Energy* **2019**, *38*, 13143. [CrossRef]
15. Carneiro, M.T.; Barros, A.Z.B.; Morais, A.I.S.; Carvalho Melo, A.L.F.; Bezerra, R.D.S.; Osajima, J.A.; Silva-Filho, E.C. Application of Water Hyacinth Biomass (*Eichhornia crassipes*) as an Adsorbent for Methylene Blue Dye from Aqueous Medium: Kinetic and Isothermal Study. *Polymers* **2022**, *14*, 2732. [CrossRef] [PubMed]
16. Amorim, D.J.; Rezende, H.C.; Oliveira, É.L.; Almeida, I.L.S.; Coelho, N.M.M.; Matos, T.N.; Araújo, C.S.T. Characterization of Pequi (*Caryocar brasiliense*) Shells and Evaluation of Their Potential for the Adsorption of Pb$^{II}$ Ions in Aqueous Systems. *J. Braz. Chem. Soc.* **2016**, *27*, 616–623. [CrossRef]
17. Borba, L.L.; Cuba, R.M.F.; Terán, F.J.C.; Castro, M.N.; Mendes, T.A. Use of Adsorbent Biochar from Pequi (*Caryocar brasiliense*) Husks for the Removal of Commercial Formulation of Glyphosate from Aqueous Media. *Braz. Arch. Biol. Technol.* **2019**, *62*, e19180450. [CrossRef]
18. Melo, A.L.F.C.; Carneiro, M.T.; Nascimento, A.M.S.S.; Morais, A.I.S.; Bezerra, R.D.S.; Viana, B.C.; Osajima, J.A.; Silva-Filho, E.C. Biochar Obtained from *Caryocar brasiliense* Endocarp for Removal of Dyes from the Aqueous Medium. *Materials* **2022**, *15*, 9076. [CrossRef]
19. Nascimento-Silva, N.R.R.D.; Naves, M.M.V. Potential of Whole Pequi (*Caryocar* spp.) Fruit-Pulp, Almond, Oil, and Shell-as a Medicinal Food. *J. Med. Food* **2019**, *22*, 952–962. [CrossRef]
20. Ramos, J.P.; Pavão, M.F.U.; Barra, E.C.; Vilhena, K.S.S.; Gouveia, F.P. Potencial de Adsorção Do Resíduo Proveniente Do Processo de Obtenção Do Silício Metálico. *Rev. Virtual Quim.* **2017**, *9*, 751–763. [CrossRef]
21. Santos, D.H.S.; Santos, J.P.T.S.; Duarte, J.L.S.; Oliveira, L.M.T.M.; Tonholo, J.; Meili, L.; Zanta, C.L.P.S. Regeneration of Activated Carbon Adsorbent by Anodic and Cathodic Electrochemical Process. *Process Saf. Environ. Prot.* **2022**, *159*, 1150–1163. [CrossRef]
22. da Silva, L.H.P.; Pinto, L.C.L.; de Melo Teixeira, S.A.; Drumond, M.A. Pequi Fruit (*Caryocar brasiliense*) in Minas Gerais: Commercialization and Public Policy. *Floresta E Ambiente* **2020**, *27*, e20171129. [CrossRef]
23. Cazetta, A.L.; Vargas, A.M.M.; Nogami, E.M.; Kunita, M.H.; Guilherme, M.R.; Martins, A.C.; Silva, T.L.; Moraes, J.C.G.; Almeida, V.C. NaOH-Activated Carbon of High Surface Area Produced from Coconut Shell: Kinetics and Equilibrium Studies from the Methylene Blue Adsorption. *Chem. Eng. J.* **2011**, *174*, 117–125. [CrossRef]
24. Mu, Y.; Ma, H. NaOH-Modified Mesoporous Biochar Derived from Tea Residue for Methylene Blue and Orange II Removal. *Chem. Eng. Res. Des.* **2021**, *167*, 129–140. [CrossRef]

25.	Ferreira, F.J.L.; Silva, L.S.; da Silva, M.S.; Osajima, J.A.; Meneguin, A.B.; Santagneli, S.H.; Barud, H.S.; Bezerra, R.D.S.; Silva-Filho, E.C. Understanding Kinetics and Thermodynamics of the Interactions between Amitriptyline or Eosin Yellow and Aminosilane-Modified Cellulose. *Carbohydr. Polym.* **2019**, *225*, 115246. [CrossRef]
26.	Lagergren, S.K. About the Theory of So-Called Adsorption of Soluble Substances. *Sven. Vetenskapsakad. Handingarl* **1898**, *24*, 1–39.
27.	Ho, Y.S.; Mckay, G. Pseudo-Second Order Model for Sorption Processes. *Process Biochem.* **1999**, *34*, 451–465. [CrossRef]
28.	Langmuir, I. The Adsorption of Gases on Plane Surfaces of Glass, Mica and Platinum. *J. Am. Chem. Soc.* **1918**, *40*, 1361–1403. [CrossRef]
29.	Freundlich, H. Über Die Adsorption in Lösungen. *Z. Für Phys. Chem.* **1907**, *57*, 385–470. [CrossRef]
30.	Chen, J.; Wang, M.; Wang, S.; Li, X. Hydrogen Production via Steam Reforming of Acetic Acid over Biochar-Supported Nickel Catalysts. *Int. J. Hydrog. Energy* **2018**, *43*, 18160–18168. [CrossRef]
31.	Chen, W.; Li, K.; Chen, Z.; Xia, M.; Chen, Y.; Yang, H.; Chen, X.; Chen, H. A New Insight into Chemical Reactions between Biomass and Alkaline Additives during Pyrolysis Process. *Proc. Combust. Inst.* **2021**, *38*, 3881–3890. [CrossRef]
32.	Jiang, D.; Li, H.; Cheng, X.; Ling, Q.; Chen, H.; Barati, B.; Yao, Q.; Abomohra, A.; Hu, X.; Bartocci, P.; et al. A Mechanism Study of Methylene Blue Adsorption on Seaweed Biomass Derived Carbon: From Macroscopic to Microscopic Scale. *Process Saf. Environ. Prot.* **2023**, *172*, 1132–1143. [CrossRef]
33.	Liu, J.; Cheng, W.; Yang, X.; Bao, Y. Modification of Biochar with Silicon by One-Step Sintering and Understanding of Adsorption Mechanism on Copper Ions. *Sci. Total Environ.* **2020**, *704*, 135252. [CrossRef] [PubMed]
34.	Li, B.; Yang, L.; Wang, C.; Zhang, Q.; Liu, Q.; Li, Y.; Xiao, R. Adsorption of Cd(II) from Aqueous Solutions by Rape Straw Biochar Derived from Different Modification Processes. *Chemosphere* **2017**, *175*, 332–340. [CrossRef]
35.	Yan, Q.; Li, J.; Cai, Z. Preparation and Characterization of Chars and Activated Carbons from Wood Wastes. *Carbon Lett.* **2021**, *31*, 941–956. [CrossRef]
36.	Zhang, X.; Mao, X.; Pi, L.; Wu, T.; Hu, Y. Adsorptive and Capacitive Properties of the Activated Carbons Derived from Pig Manure Residues. *J. Environ. Chem. Eng.* **2019**, *7*, 103066. [CrossRef]
37.	Xu, Z.; He, M.; Xu, X.; Cao, X.; Tsang, D.C.W. Impacts of Different Activation Processes on the Carbon Stability of Biochar for Oxidation Resistance. *Bioresour. Technol.* **2021**, *338*, 125555. [CrossRef]
38.	Li, C.; Zhang, X.; Lv, Z.; Wang, K.; Sun, X.; Chen, X.; Ma, Y. Scalable Combustion Synthesis of Graphene-Welded Activated Carbon for High-Performance Supercapacitors. *Chem. Eng. J.* **2021**, *414*, 128781. [CrossRef]
39.	Mohammed, A.A.; Chen, C.; Zhu, Z. Low-Cost, High-Performance Supercapacitor Based on Activated Carbon Electrode Materials Derived from Baobab Fruit Shells. *J. Colloid. Interface Sci.* **2019**, *538*, 308–319. [CrossRef]
40.	Ren, Z.; Wang, Z.; Lv, L.; Ma, P.; Zhang, G.; Li, Y.; Qin, Y.; Wang, P.; Liu, X.; Gao, W. Fe–N Complex Biochar as a Superior Partner of Sodium Sulfide for Methyl Orange Decolorization by Combination of Adsorption and Reduction. *J. Environ. Manag.* **2022**, *316*, 115213. [CrossRef]
41.	Feng, D.; Guo, D.; Zhang, Y.; Sun, S.; Zhao, Y.; Shang, Q.; Sun, H.; Wu, J.; Tan, H. Functionalized Construction of Biochar with Hierarchical Pore Structures and Surface O-/N-Containing Groups for Phenol Adsorption. *Chem. Eng. J.* **2021**, *410*, 127707. [CrossRef]
42.	Ye, J.; Tao, S.; Zhao, S.; Li, S.; Chen, S.; Cui, Y. Characteristics of Methane Adsorption/Desorption Heat and Energy with Respect to Coal Rank. *J. Nat. Gas. Sci. Eng.* **2022**, *99*, 104445. [CrossRef]
43.	Zhu, H.; Liu, X.; Jiang, Y.; Zhang, M.; Lin, D.; Yang, K. Time-Dependent Desorption of Anilines, Phenols, and Nitrobenzenes from Biochar Produced at 700 °C: Insight into Desorption Hysteresis. *Chem. Eng. J.* **2021**, *422*, 130584. [CrossRef]
44.	Eltaweil, A.S.; Ali Mohamed, H.; Abd El-Monaem, E.M.; El-Subruiti, G.M. Mesoporous Magnetic Biochar Composite for Enhanced Adsorption of Malachite Green Dye: Characterization, Adsorption Kinetics, Thermodynamics and Isotherms. *Adv. Powder Technol.* **2020**, *31*, 1253–1263. [CrossRef]
45.	Wang, T.; Zheng, J.; Cai, J.; Liu, Q.; Zhang, X. Visible-Light-Driven Photocatalytic Degradation of Dye and Antibiotics by Activated Biochar Composited with K+ Doped g-C$_3$N$_4$: Effects, Mechanisms, Actual Wastewater Treatment and Disinfection. *Sci. Total Environ.* **2022**, *839*, 155955. [CrossRef]
46.	Carneiro, M.T.; Morais, A.Í.S.; de Carvalho Melo, A.L.F.; Ferreira, F.J.L.; Santos, F.E.P.; Viana, B.C.; Osajima, J.A.; Bezerra, R.D.S.; Del Mar Orta Cuevas, M.; Peña-Garcia, R.R.; et al. Biochar Derived from Water Hyacinth Biomass Chemically Activated for Dye Removal in Aqueous Solution. *Sustainability* **2023**, *15*, 14578. [CrossRef]
47.	Doğan, M.; Sabaz, P.; Bïcïl, Z.; Koçer Kizilduman, B.; Turhan, Y. Activated Carbon Synthesis from Tangerine Peel and Its Use in Hydrogen Storage. *J. Energy Inst.* **2020**, *93*, 2176–2185. [CrossRef]
48.	Jawad, A.H.; Abdulhameed, A.S.; Mastuli, M.S. Acid-Factionalized Biomass Material for Methylene Blue Dye Removal: A Comprehensive Adsorption and Mechanism Study. *J. Taibah Univ. Sci.* **2020**, *14*, 305–313. [CrossRef]
49.	Suhaimi, N.; Kooh, M.R.R.; Lim, C.M.; Chou Chao, C.-T.; Chou Chau, Y.-F.; Mahadi, A.H.; Chiang, H.-P.; Haji Hassan, N.H.; Thotagamuge, R. The Use of Gigantochloa Bamboo-Derived Biochar for the Removal of Methylene Blue from Aqueous Solution. *Adsorpt. Sci. Technol.* **2022**, *2022*, 8245797. [CrossRef]
50.	Kooh, M.R.R.; Thotagamuge, R.; Chou Chau, Y.-F.; Mahadi, A.H.; Lim, C.M. Machine Learning Approaches to Predict Adsorption Capacity of Azolla Pinnata in the Removal of Methylene Blue. *J. Taiwan. Inst. Chem. Eng.* **2022**, *132*, 104134. [CrossRef]
51.	Bernal-Romero del Hombre Bueno, M.D.L.Á.; Boluda-Botella, N.; Prats Rico, D. Removal of Emerging Pollutants in Water Treatment Plants: Adsorption of Methyl and Propylparaben onto Powdered Activated Carbon. *Adsorption* **2019**, *25*, 983–999. [CrossRef]
52.	Yin, Y.; Zhou, T.; Luo, H.; Geng, J.; Yu, W.; Jiang, Z. Adsorption of Arsenic by Activated Charcoal Coated Zirconium-Manganese Nanocomposite: Performance and Mechanism. *Colloids Surf. A Physicochem. Eng. Asp.* **2019**, *575*, 318–328. [CrossRef]

53. Paschalidou, P.; Pashalidis, I.; Manariotis, I.D.; Karapanagioti, H.K. Hyper Sorption Capacity of Raw and Oxidized Biochars from Various Feedstocks for U(VI). *J. Environ. Chem. Eng.* **2020**, *8*, 103932. [CrossRef]

54. Liu, S.; Shen, C.; Wang, Y.; Huang, Y.; Hu, X.; Li, B.; Karnowo; Zhou, J.; Zhang, S.; Zhang, H. Development of $CO_2/H_2O$ Activated Biochar Derived from Pine Pyrolysis: Application in Methylene Blue Adsorption. *J. Chem. Technol. Biotechnol.* **2022**, *97*, 885–893. [CrossRef]

55. Qiu, B.; Shao, Q.; Shi, J.; Yang, C.; Chu, H. Application of Biochar for the Adsorption of Organic Pollutants from Wastewater: Modification Strategies, Mechanisms and Challenges. *Sep. Purif. Technol.* **2022**, *300*, 121925. [CrossRef]

56. Yang, Y.; Sun, C.; Huang, Q.; Yan, J. Hierarchical Porous Structure Formation Mechanism in Food Waste Component Derived N-Doped Biochar: Application in VOCs Removal. *Chemosphere* **2022**, *291*, 132702. [CrossRef]

57. Sajjadi, B.; Chen, W.Y.; Egiebor, N.O. A Comprehensive Review on Physical Activation of Biochar for Energy and Environmental Applications. *Rev. Chem. Eng.* **2019**, *35*, 735–776. [CrossRef]

58. Sajjadi, B.; Broome, J.W.; Chen, W.Y.; Mattern, D.L.; Egiebor, N.O.; Hammer, N.; Smith, C.L. Urea Functionalization of Ultrasound-Treated Biochar: A Feasible Strategy for Enhancing Heavy Metal Adsorption Capacity. *Ultrason. Sonochem* **2019**, *51*, 20–30. [CrossRef]

59. Kar, S.; Santra, B.; Kumar, S.; Ghosh, S.; Majumdar, S. Sustainable Conversion of Textile Industry Cotton Waste into P-Dopped Biochar for Removal of Dyes from Textile Effluent and Valorisation of Spent Biochar into Soil Conditioner towards Circular Economy. *Environ. Pollut.* **2022**, *312*, 120056. [CrossRef]

60. dos Santos, K.J.L.; dos Santos, G.E.d.S.; de Sá, Í.M.G.L.; Ide, A.H.; Duarte, J.L.d.S.; de Carvalho, S.H.V.; Soletti, J.I.; Meili, L. *Wodyetia bifurcata* Biochar for Methylene Blue Removal from Aqueous Matrix. *Bioresour. Technol.* **2019**, *293*, 122093. [CrossRef]

61. Jabar, J.M.; Odusote, Y.A. Utilization of Prepared Activated Biochar from Water Lily (*Nymphaea lotus*) Stem for Adsorption of Malachite Green Dye from Aqueous Solution. *Biomass Convers. Biorefin.* **2021**. [CrossRef]